ACS Catalysis

Research Article

pubs.acs.org/acscatalysis

Graphene-Supported, Iron-Based Nanoparticles for Catalytic Production of Liquid Hydrocarbons from Synthesis Gas: The Role of the Graphene Support in Comparison with Carbon Nanotubes

Sherif O. Moussa, Leela S. Panchakarla, Minh Q. Ho, and M. Samy El-Shall*,†

Department of Chemistry, Virginia Commonwealth University, Richmond, Virginia 23284, United States

Supporting Information

ABSTRACT: Fischer–Tropsch synthesis (FTS) is a potentially attractive technology for the production of clean liquid fuels from synthesis gas. The efficiency and selectivity of FTS can be enhanced by the design of new active catalyst systems with improved selectivity for long-chain hydrocarbons and low methane production. In this paper, we introduce a new class of FT catalysts supported on the high surface area graphene nanosheets and report on their high activity and selectivity for the production of long-chain hydrocarbons. The chemical reduction of graphene oxide in water in the presence of the metal salts under microwave irradiation allows the deposition of well-dispersed surface-oxidized metal nanoparticles on the defect sites of the graphene nanosheets. The Fe–K-nanoparticle catalyst supported on graphene exhibits high activity and selectivity toward C_8 and higher hydrocarbons with excellent stability and recyclability. In comparison with other carbon supports, such as carbon nanotubes, the graphene support shows a unique tendency for minor formation of the low-value and undesirable products methane and carbon dioxide, respectively. The water-gas shift activity is reduced on the graphene support as compared with CNTs, and as a result, the formation of CO_2 is significantly reduced. Evidence is presented for the formation of the active Fe_5C_2 iron carbide phase during the FTS on the graphene-supported Fe catalysts. The high activity and selectivity of the catalysts supported on graphene are correlated with the presence of defects within the graphene lattice that act as favorable nucleation sites to anchor the metal nanoparticles, thus providing tunable metal–support interactions. Given the activity, selectivity, and stability of the new graphene-supported, Fe-based nanoparticle catalysts, their industrial application appears to be promising. Controlling the nature and density of the defect sites in graphene could lead to improved understanding of the catalyst–graphene interactions and to further enhancement of the performance of these catalysts for the production of liquid fuels.

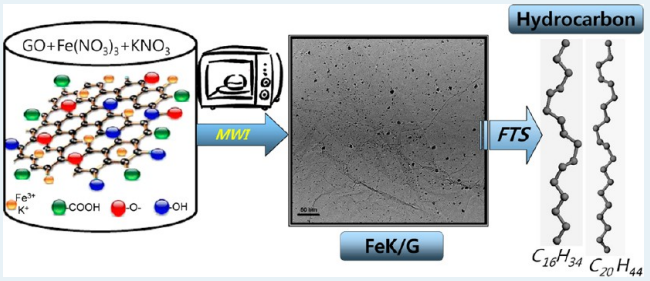

KEYWORDS: *graphene, iron-based catalysts, Fischer–Tropsch, microwave synthesis, graphene defects, Raman spectra of Fe–graphene catalysts*

INTRODUCTION

Growing worldwide energy demand, high commodity prices, high economic growth in developing countries, and growing scientific evidence that atmospheric carbon dioxide is among the most important contributors to global climate change make it urgent to increase energy supply and reduce worldwide greenhouse gas emissions at the same time.[1−3] Biomass is a renewable resource and, if properly produced and converted, can yield liquid fuels that have lower greenhouse gas emissions than do petroleum-based gasoline and diesel.[4−8] One of the well-established catalytic processes to produce liquid fuels and valuable organic compounds from the efficient gasification of biomass feedstock is the Fischer–Tropsch synthesis (FTS).[9−15] This process has a unique position in the chemical industry with huge economic incentives.[3,9] It provides a route for the production of transportation fuels and valuable chemicals from feedstocks such as coal, biomass, and natural gas as alternatives to oil.[3,9]

FTS involves the catalytic conversion of the H_2 and CO in synthesis gas (syngas) into fuel hydrocarbons, such as diesel, gasoline, and naphtha.[9−15] FT-derived diesel (C_8–C_{18} *n*-alkanes) is clean-burning and ∼30% more efficient than gasoline.[9−15] However, most of the current FT catalysts are expensive, not readily recyclable, and usually produce a wide array of hydrocarbon products in addition to CH_4, CO_2, and several oxygenates.[9−17] Because the competing formation of methane as a byproduct wastes H_2, a costly syngas component, lowering CH_4 selectivity and increasing the production of long-chain hydrocarbons (C_8+ products) are among the most important goals of developing new FTS catalyst systems.

Iron-based catalysts have great value in FTS, mostly because of their low cost, relatively high activity over a wide

Received: November 3, 2013
Revised: December 19, 2013
Published: December 24, 2013

temperature range (220−350 °C) to produce diesel in low temperature or gasoline components in high temperature FTS, and their ability to catalyze the water-gas shift reaction (WGS), thus enabling the production of liquid hydrocarbons from syngas with a low H_2-to-CO ratio as in biomass and coal sources where the H_2/CO ratio is ∼1.[15,18−29] Most of the iron-based FT catalysts have been supported on high-surface-area oxides, such as SiO_2, Al_2O_3, TiO_2, MgO, and zeolites.[9,10,15,18,21−24,27,28] However, it is well-known that iron forms mixed oxides when supported on silica or alumina due to the influence of strong metal−support interactions, which result in the formation of iron silicate or iron aluminate, which are difficult to reduce, and therefore, the formation of the active Fe carbide phase may be hindered.[18,23,30,31] Furthermore, the lack of selectivity of the current FT catalysts imposes expensive separation, upgrading, and purification processes, which contribute to the high cost of the liquid fuels produced by the FTS. Therefore, the development of a new generation of FT nanocatalysts that combine high activity, selectivity, stability, and recyclability is an extremely important goal of heterogeneous catalysis research that is likely to have a considerable impact on fuel and chemical industries in the near future.[3−7]

Recent attempts to develop highly efficient and selective FT catalysts have focused on using nanocarbon materials, such as carbon nanofibers and carbon nanotubes (CNTs), as support systems for the iron- and cobalt-based catalysts.[29,31−42] In fact, nanocarbon materials are becoming an emerging field in the development of advanced supported catalysts because they provide limited interaction with the metal catalysts and, in some cases, could provide tunable catalyst−support interactions.[43,44] For example, carbon nanofibers have been recently used to develop highly selective catalysts for the production of low olefins from syngas by the so-called FTO or FT-to-olefins process.[29,31,34] In addition, a number of studies have reported higher activity in FTS by using CNTs as a support for the iron-based catalysts to produce long-chain hydrocarbons.[35−42] However, the major problem in using CNTs as a support is the large variation in the catalyst activity, depending on the deposition of the metal nanoparticles inside or outside the nanotubes, and the sharp dependence of the activity on the diameters of the tubes combined with the high cost of CNTs.[35−42] On the other hand, a recent study has incorporated iron nanoparticles into graphene oxide as FTS catalysts and demonstrated that residual oxygen species in graphene oxide can suppress the FTS activity and chain growth probability, thus requiring annealing the catalysts in hydrogen at temperatures as high as 800 °C to enhance the FTS activity.[45] These studies signify the need for a new approach to develop active, selective, and economically viable supported FTS catalysts.[3]

In this paper, we report, for the first time, the application of graphene (used here as reduced graphene oxide) as a high surface area support (2600 m^2g^{-1}, theoretical value) for Fe-based nanoparticle catalysts for the production of long-chain hydrocarbons by the FTS. Recently, graphene has shown unique properties and remarkable tunability in supporting a variety of metallic and bimetallic nanoparticle catalysts in heterogeneous catalysis.[46−51] As a working hypothesis, we postulated that the defect sites incorporated in the sp^2-bonded carbon network of graphene would impart thermal stability against particle growth to the iron-based catalysts without inhibiting their activation. Because of the well-defined structure of graphene, it is potentially possible to have more-defined and -controlled types of defects that can be better tuned to have the necessary catalytic functionalities or surface properties.[44] Furthermore, because of the extended π-system in graphene and the high electron density, it may be easier to reduce metal oxide nanoparticles, such as iron or cobalt oxides, on the surface of graphene, thus generating catalytically active metal centers anchored to the graphene support. Graphene could also enhance the formation of the active phase of the iron-based FT catalysts, which could influence the catalyst activity and product selectivity.

In this paper, we report an innovative approach for the design and synthesis of efficient, selective, and recyclable iron-based nanoparticle catalysts supported on graphene nanosheets. We use the microwave irradiation (MWI)-assisted reduction method recently developed for the reduction of graphene oxide (GO) and for the synthesis of metal nanoparticles supported on graphene.[48,51,52] This method provides a homogeneous distribution of the iron-based nanoparticles within the surface of the graphene support. The main advantage of MWI over other conventional heating methods is the rapid and uniform heating of the reaction mixture.[52−54] Because of the difference in the solvent and reactant dielectric constants, selective dielectric heating can provide significant enhancement in the transfer of energy directly to the reactants, which causes an instantaneous internal temperature rise.[52−54] This temperature rise in the presence of an appropriate chemical reducing agent allows the simultaneous reduction of the metal ions and GO and the dispersion of the metal nanoparticles on the large surface area of the resulting graphene nanosheets.[48,51,52] The nonequilibrium dielectric heating of GO is expected to result in the formation of structural defects in the resulting graphene lattice. These defect sites act as nucleation centers for the formation of surface-oxidized iron nanoparticles anchored to the graphene sheets, thus providing intermediate metal−support interaction. We have studied unpromoted, K-promoted, Mn-promoted, and K−Mn-promoted Fe-based catalysts supported on graphene. We use the K-promoted catalyst for a comparison with CNT as another nanocarbon support system.

EXPERIMENTAL SECTION

Preparation of Graphene Oxide Nanosheets. In the experiments, GO was prepared by the oxidation of high-purity graphite powder (99.9999%, 200 mesh, Alfa Aesar) according to the method of Hummers and Offeman.[55] After repeated washing of the resulting yellowish-brown cake with hot water, it was dried at room temperature under vacuum overnight. Two milligrams of the dried GO was sonicated in 10 mL of deionized water until a homogeneous yellow dispersion was obtained.

Preparation of Iron-Based Nanoparticle Catalysts Supported on Graphene. The catalysts were prepared by reduction of metal nitrates and GO in aqueous dispersions using hydrazine hydrate (HH) as a reducing agent under MWI. Prior to the FTS experiments, further reduction of the catalyst was carried out in pure H_2 at 450 °C for 3 h. The FTS was carried out at a temperature of 325 °C and a total pressure of 1.5 MPa. Details regarding preparation, procedure, and product analysis of the graphene-supported Fe-based nanoparticle catalysts can be found in the Supporting Information (SI).

Preparation of Iron-Based Nanoparticle Catalysts Supported on f-CNTs. CNTs were prepared by placing 1 g of ferrocene in a ceramic boat located at one end of a quartz

dx.doi.org/10.1021/cs4010198 | ACS Catal. 2014, 4, 535−545

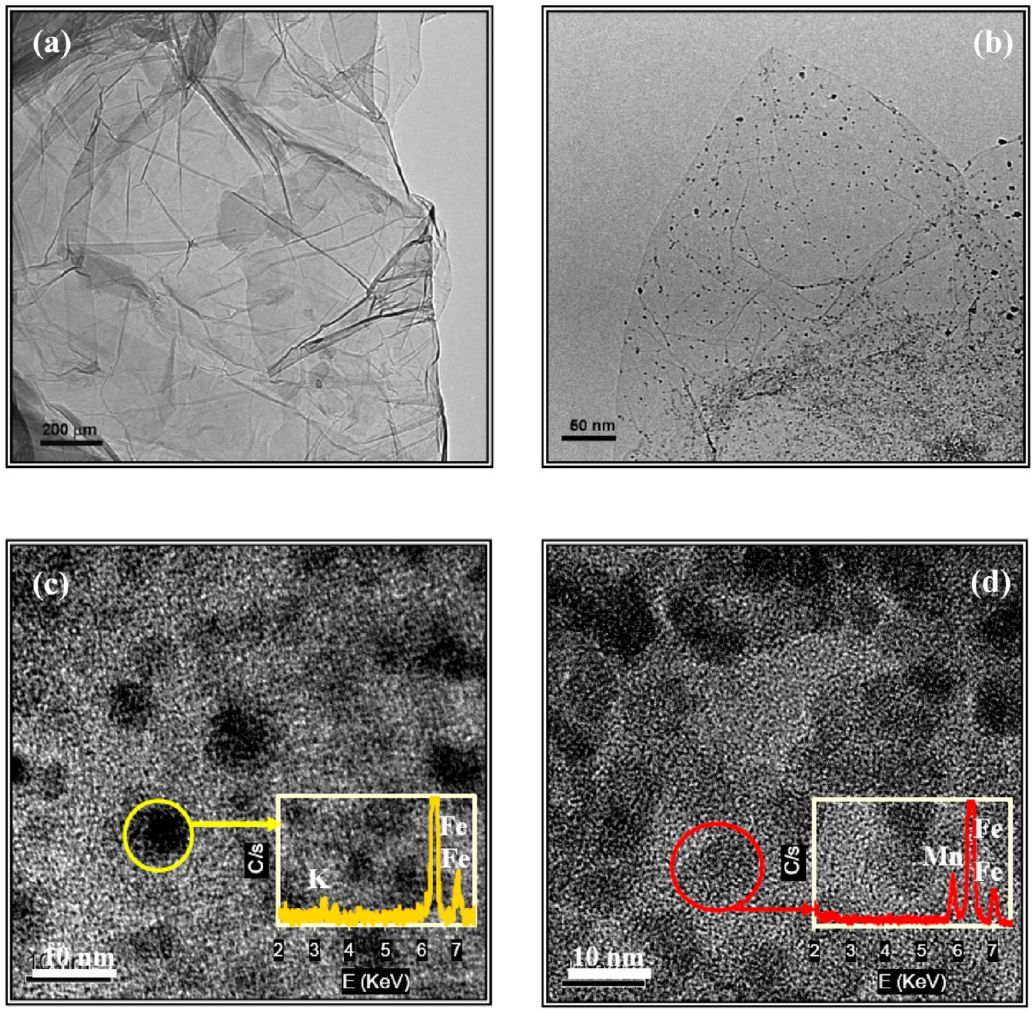

Figure 1. TEM images of (a) graphene (G), (b) Fe15-G, (c) Fe15K5-G, and (d) Fe15Mn5-G catalysts prepared by 2 min MWI-HH reduction. EDX analyses are shown in parts c and d.

tube in a duel furnace system (SI, Figure S1).[56] The ferrocene was sublimed by raising the temperature of the first furnace to 350 °C at a heating rate of 20 °C/min.[56] Argon was used as a carrier gas for carrying the ferrocene vapor into the second furnace, and ethylene was used to provide an additional carbon source. Ethylene was admitted into the reaction tube just before the sublimation of ferrocene. The flow rates of the gases were controlled. Pyrolysis took place inside the second furnace, and its temperature was maintained constant at 950 °C. Pyrolysis yielded copious quantities of carbon nanotubes deposited at the center and outlet of the second furnace. The samples collected from the interior of the quartz reaction tube consisted of iron-encapsulated carbon nanotubes. The as-prepared carbon nanotubes were refluxed in 10 M HNO_3 acid to functionalize their edges and surfaces with carboxylic and hydroxyl groups. The f-CNTs were filtered and washed several times with distilled water until the pH was 7. The f-CNTs were used to prepare the $Fe_{15}K_5$-CNTs and $Fe_{15}K_5$-50%G-50%f-CNTs catalysts using HH-MWI under the same experimental conditions used to prepare the $Fe_{15}K_5$-G catalyst.

Catalyst Characterization. TEM images were obtained using a Jeol JEM-1230 electron microscope operated at 120 kV equipped with a Gatan UltraScan 4000SP 4K × 4K CCD camera. SEM images were carried out using a Quantum DS-130S dual stage electron microscope. The small-angle X-ray diffraction (SA-XRD) patterns were measured at room temperature with an X'Pert Philips Materials Research Diffractometer using Cu Kα1 radiation. The reducibility of Fe_2O_3 nanoparticles supported on graphene was studied by temperature-programed reduction in H_2 (H_2-TPR, Micromeritics AutochemII) by heating the sample in flowing 10% H_2/Ar up to 600 °C at a rate of 2 °C/min. The X-ray photoelectron spectroscopy (XPS) spectra were measured on a Thermo Fisher Scientific ESCALAB 250 using a monochromatic Al KR. The Raman spectra were measured using an excitation wavelength of 407 nm provided by a Spectra-Physics model 2025 argon ion laser. The laser beam was focused to a 0.10 mm diameter spot on the sample with a laser power of 1 mW. The sample was pressed into a depression at the end of a 3 mm diameter stainless steel rod, and held at a 30° angle in the path of the laser beam. The detector was a Princeton Instruments 1340 × 400 liquid nitrogen CCD detector attached to a Spex model 1870 0.5 m single spectrograph with interchangeable 1200 and 600 lines/mm holographic gratings (Jobin-Yvon). The Raman scattered light was collected by a Canon 50 mm f/0.95 camera lens. Though the holographic gratings provided high discrimination, Schott and Corning glass cutoff filters were used to provide additional filtering of reflected laser light when necessary.

dx.doi.org/10.1021/cs4010198 | ACS Catal. 2014, 4, 535−545

RESULTS AND DISCUSSION

Iron-Based Catalysts Supported on Graphene. Figure 1a displays a typical TEM image of the graphene (G) nanosheets produced by the hydrazine hydrate (HH)-MWI reduction of GO.[52] Figure 1b, c, and d show representative TEM images of the Fe_{15}-G (15 wt % Fe), $Fe_{15}K_5$-G (15 wt % Fe and 5 wt % K), and $Fe_{15}Mn_5$-G (15 wt % Fe and 5 wt % Mn) catalysts prepared by the reduction of the respective metal nitrates [$Fe(NO_3)_3$, $Fe(NO_3)_3$ + KNO_3, and $Fe(NO_3)_3$ + $Mn(NO_3)_2$, respectively] mixed with the aqueous GO dispersion using HH as a reducing agent under MWI. Most of the reduction of the metal ions, especially K^+ and Mn^{2+}, takes place during the drying and activation steps (SI). In all cases, well-dispersed metal nanoparticles with an average size of 4−6 nm are formed (Figures S2, S3, and S4; SI). The presence of K as a promoter results in a bimodal size distribution with 80% of the particles with an average size of 3−5 nm and 20% with an average size of 10−14 nm (SI Figure S4). Energy-dispersive X-ray spectroscopy (EDX) confirms the presence of Fe and K in the $Fe_{15}K_5$-G catalyst and Fe and Mn in the $Fe_{15}Mn_5$-G catalyst, as shown in Figure 1c and d, respectively.

The XRD patterns of the as-prepared graphene-supported catalysts show complete disappearance of the diffraction peak of GO at 2θ = 10.9°, indicating the exfoliation and reduction of GO nanosheets (Figure S5, SI). The reduction of GO is confirmed by the XPS spectra of the C 1s electron binding energies of the as-prepared catalysts. (Figure S6-a, SI). The results also indicate the formation of an amorphous surface layer of oxidized Fe, Fe−K, and Fe−Mn nanoparticles supported on graphene in the as-prepared catalysts. Specifically, the XPS spectra of the Fe 2p and Mn 2p electrons confirm the presence of the surface oxide layers Fe_2O_3 and MnO on the Fe and Fe−Mn catalysts, respectively, in the as-prepared catalysts (Figures S6-b, S7-b, and S7-c; SI). XRD data obtained following the activation of the as-prepared catalysts in H_2 at 450 °C for 3 h clearly show the presence of metallic iron (Figures S8 and S9; SI). Because of the thermal stability of graphene up to 800 °C,[48,52] no gasification of graphene is observed during the catalyst activation process at 450 °C.

TPR analysis was performed to evaluate the reduction of the Fe_2O_3 nanoparticles on the graphene surface. Figure 2 shows the H_2-TPR pattern for the Fe_{15}-G (15 wt % Fe) catalyst where three reduction peaks can be identified around 300−320, 400−420, and 520 °C, corresponding to the reduction of Fe_2O_3 first to Fe_3O_4, then to FeO, and finally to metallic Fe, respectively. These reduction temperatures are significantly lower than those found for the reduction of Fe_2O_3 nanoparticles dispersed on the outer walls of CNTs (inner and outer diameters of 4−8 and 10−20 nm, respectively),[39] where the emergence and disappearance of FeO appear at 455 and 620 °C, respectively, and the emergence and full development of the metallic Fe XRD peak occur at 470 and 620 °C, respectively.[39] However, the reduction peaks of Fe_2O_3 on graphene shown in Figure 2 are nearly similar to those occurring when the Fe_2O_3 nanoparticles are incorporated inside the channels of CNTs, where the emergence and full development of the metallic Fe peak occur at 390 and 565 °C, respectively.[39] In fact, the reduction peak corresponding to the formation of metallic Fe on graphene occurs in Fe_{15}-G (Figure 2) at ∼45 °C lower than that for the encapsulated Fe_2O_3 catalyst inside CNTs with inner diameters of 4−8 nm.[39] A similar trend is found in comparing the TPR of Fe_2O_3 nanoparticles inside wider CNTs with diameters of 12 and 63 nm, where the formation of metallic Fe was observed at 667 and 574 °C, respectively,[41] as compared wtih 520 °C for the current Fe_2O_3 nanoparticles supported on graphene. This suggests that the Fe_2O_3 nanoparticles can be more easily reduced on graphene than on CNTs, probably bcause of the extended π-system and high π-electron density of graphene, which could assist in the reduction process.

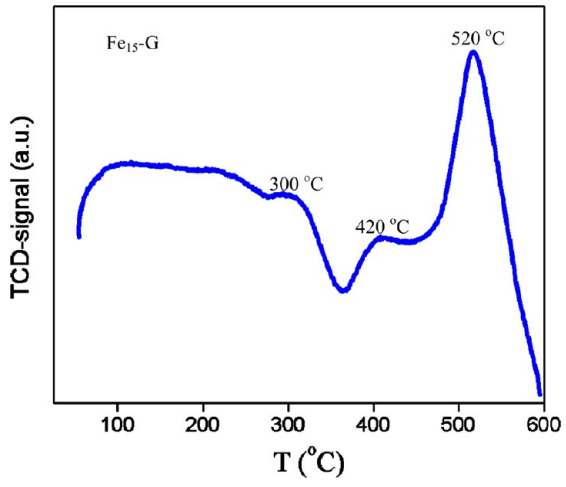

Figure 2. H2-TPR of Fe15-G catalyst under 10% H2−90% Ar atmosphere.

Flow-Reactor Studies. Figure 3 presents the FT catalysis results over the reduced Fe_{15}-G, $Fe_{15}K_5$-G, $Fe_{15}Mn_5$-G, and $Fe_{15}K_5Mn_5$-G catalysts under the same conditions of reaction temperature (325 °C) and pressure (1.5 MPa) (description of the flow reactor and conditions of the reactions are given in the SI, Figure S10). Several interesting observations can be directly established and correlated with the composition and concentration of the Fe-based nanoparticles supported on graphene. First, the CO conversion increases within the first 20 h on-stream and reaches a constant value at 40 h with no further change over the 80 h reaction time, reaching maximum conversions of 51.5%, 73.5%, 92%, and 90% for the Fe_{15}-G, $Fe_{15}K_5$-G, $Fe_{15}Mn_5$-G, and $Fe_{15}Mn_5K_5$-G catalysts under the same space velocity of 2500 cm^3 (STP)/(h g), as shown in Figure 3a. This behavior is in contrast with most of the FT Fe-based catalysts supported on CNTs or on carbon spheres, where an initial high activity was observed within a short time on-stream (10 h), followed by a decrease in the CO conversion, depending on the nature of the support system.[40,41,57] For example, CO conversion on Fe catalysts supported on narrow pore (12 nm) and wide pore (63 nm) CNTs dropped from 31% to 26% and from 18% to 9%, respectively, over a period of 120 h at a temperature of 275 °C and a pressure of 2 MPa.[41] With narrower CNTs (5−12 nm), higher CO conversion of 89% and 91% with a small drop to 85% and 79% was observed for the Fe catalysts inside and outside the CNTs, respectively, in a period of 125 h at a temperature of 270 °C and a pressure of 2 MPa.[40] Recently, Fe_xO_y catalysts supported on large carbon spheres (6 μm) showed 76% CO conversion after 70 h on-stream at a temperature of 270 °C and a pressure of 2 MPa.[57] In general, it can be concluded that the CO conversion efficiency of the current graphene-supported Fe catalysts is higher or comparable to the best Fe-based catalysts supported outside and inside the CNTs, respectively, as reported in the literature.[36−41]

dx.doi.org/10.1021/cs4010198 | ACS Catal. 2014, 4, 535−545

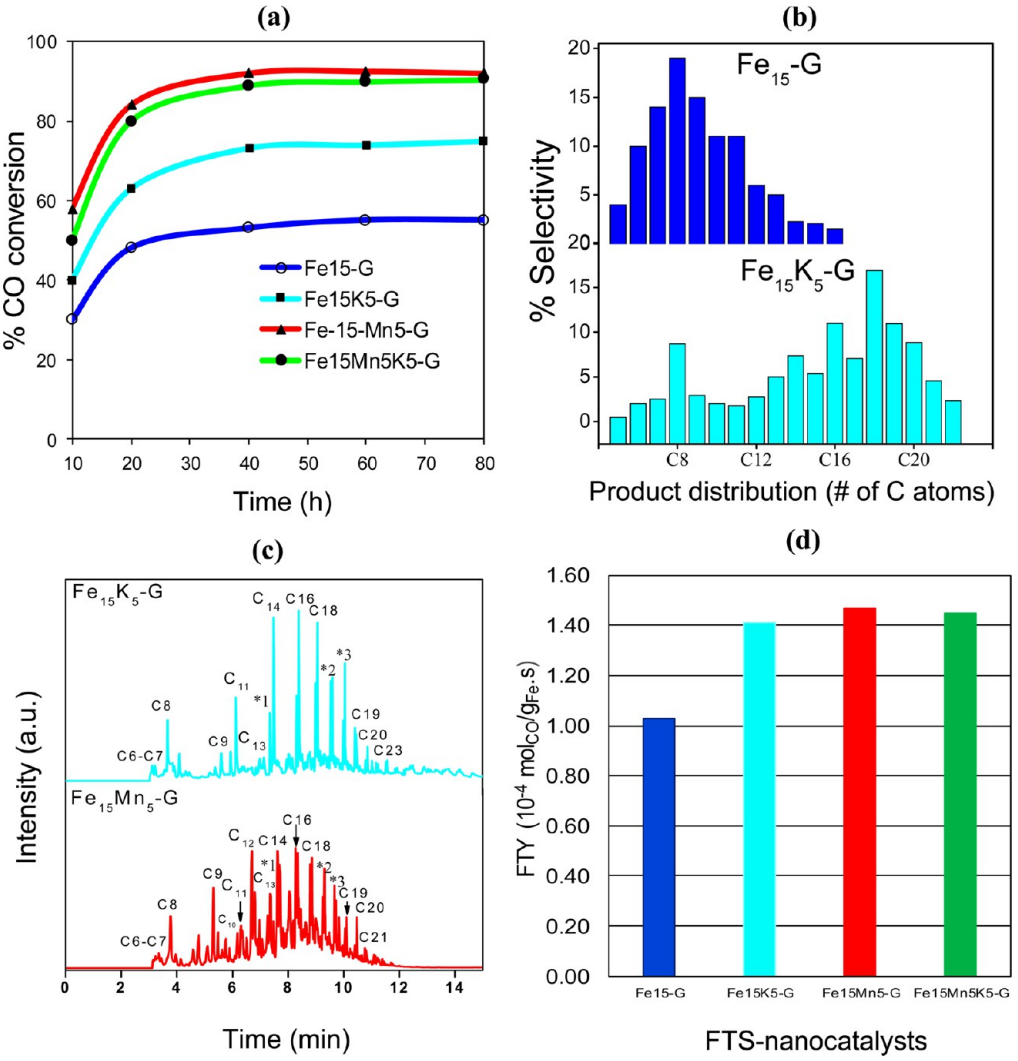

Figure 3. (a) Percent CO conversion vs time on-stream (hours) for Fe_{15}-G, $Fe_{15}K_5$-G, $Fe_{15}Mn_5$-G, and $Fe_{15}Mn_5K_5$-G catalysts at 2500 cm^3 (STP)/(h g) space velocity. (b) Comparison of the product distribution of the liquid hydrocarbons produced over Fe_{15}-G and $Fe_{15}K_5$-G catalysts after 48 h on-stream. (c) GC chromatograms of the liquid products produced by the $Fe_{15}K_5$-G and $Fe_{15}Mn_5$-G catalysts after 80 h on-stream. Peaks labeled with *1, *2, and *3 correspond to the oxygenated hydrocarbons $C_{12}H_{26}O$, $C_{15}H_{32}O$, and $C_{16}H_{34}O$ (the slight shift in retention time between the two chromatograms is due to different injection times). (d) Catalytic activities (expressed as moles of CO converted to hydrocarbons per gram of iron per second (Fe time yield, FTY) for the graphene-supported catalysts Fe_{15}-G, $Fe_{15}K_5$-G, $Fe_{15}Mn_5$-G, and $Fe_{15}Mn_5K_5$-G catalysts after 48 h on-stream. All the reactions were performed at a temperature of 325 °C and a pressure of 1.5 MPa.

The second important result revealed by the data shown in Figure 3 is the enhanced formation of long-chain hydrocarbons attributed to the presence of the K and Mn promoters, as shown in Figure 3b and c. This observation is consistent with the known effect of the K and Mn promoters, as observed in other Fe-based FT catalysts supported on high-surface-area oxides.[27,34] In addition, in both the K- and Mn-containing catalysts supported on graphene, the formation of oxygenated hydrocarbons (most probably alcohols) is observed, as shown in Figure 3c. Figure 3d compares the activities of the Fe_{15}-G, $Fe_{15}K_5$-G, $Fe_{15}Mn_5$-G, and $Fe_{15}Mn_5K_5$-G catalysts after 48 h on-stream expressed as moles of CO converted to liquid hydrocarbons (C5 and higher) per gram of iron per second, which is defined as the Fe time yield (FTY). Again, the presence of the K and Mn promoters results in a significant increase in the FTY, most likely as a result of increasing the chain growth rate.[34]

Comparison with Fe-Based Catalysts Supported on f-CNTs. To compare the activity and selectivity of the $Fe_{15}K_5$ catalyst supported on graphene with a similar catalyst supported on another carbon support, we prepared the $Fe_{15}K_5$ catalyst supported on functionalized CNTs (f-CNTs) (characterization of the catalysts supported on f-CNTs is described in the SI, Figures S11−S13). We also prepared the $Fe_{15}K_5$ catalyst supported on a mixture of 50% graphene and 50% f-CNTs. Representative TEM micrographs of the as-prepared catalysts are shown in Figure 4a and b, and SEM images of the activated catalysts (heating at 450 °C in H_2 atmosphere for 3 h) are shown in Figure 4c and d. It is clear that most of the Fe-based nanoparticles are incorporated inside the f-CNTs or well-dispersed on the surface of the graphene support. Specifically, the SEM images of the activated catalysts show well-dispersed Fe nanoparticles incorporated within a few layer graphene nanosheets (Figure 4c) or inside the f-CNTs (Figure 4d).

Table 1 summarizes the performance of all the Fe-based catalysts investigated in the present work, including the effects of the K and Mn promoters and the nature of the support

dx.doi.org/10.1021/cs4010198 | ACS Catal. 2014, 4, 535−545

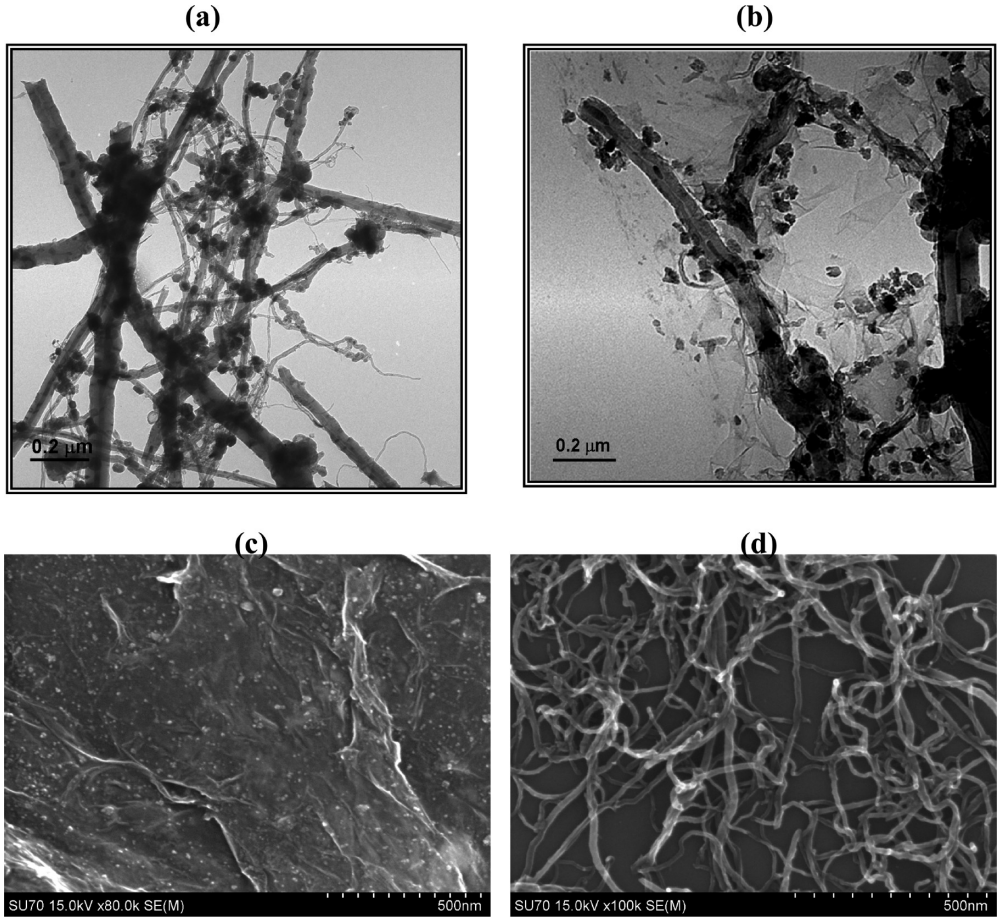

Figure 4. (a, b) TEM images of the as-prepared $Fe_{15}K_5$ nanocatalyst supported on (a) f-CNTs and (b) 50% f-CNTs/50% graphene composite. (c, d) SEM-images of the (c) $Fe_{15}K_5$-graphene and (d) the $Fe_{15}K_5$-f-CNTs catalysts after 3 h of homogenization at 450 °C in H_2 atmosphere.

Table 1. Summary of Graphene-Supported FTS-Catalyst Performance for Reactions Performed at 325 °C, 1.5 MPa, H_2/CO = 2, and 2500 cm^3 (STP)/(h g) Space Velocity after 48 h On-Stream

				product selectivity (% C_{at}, CO_2-free)		
catalyst	total CO conversion (%)	CO-to-CO_2 conversion (%)	FTY-(CO_2-free) (10^{-4} mol CO/g_{Fe} s)	CH_4	C2−C7	C8+
Fe_{15}-G	51.5	2	1.03	1.5	32.0	66.5
$Fe_{15}K_5$-G	73.5	2.6	1.40	2.6	10.7	86.7
$Fe_{15}K_5$-G[a]	70	2.4	1.15	2.7	10.5	86.8
$Fe_{20}K_{10}$-G	81.5	4	1.50	3.1	11.0	85.9
$Fe_{15}Mn_5$-G	92	9	1.47	13.5	10.0	76.5
$Fe_{15}Mn_5K_5$-G	90	7.5	1.46	8.0	12.5	79.5
$Fe_{15}K_5$−f-CNTs	84	14	1.18	11.5	27.0	61.5
$Fe_{15}K_5$−50% G−50% f-CNTs	80	9	1.32	7.6	14.0	78.4

[a]FT-catalyst weight was 1 g; all other catalysts' weight was 1.5 g.

under the same reaction conditions. As illustrated by the data shown in Figure 3 and discussed above, the presence of promoters such as K and Mn leads to a significant increase in the activity of the Fe_{15}-G catalyst, as shown by increasing the percent CO conversion from 51.5% for the Fe_{15}-G catalyst to 73.5% and 92% for the $Fe_{15}K_5$-G and $Fe_{15}Mn_5$-G catalysts, respectively. This can be attributed to improving the CO dissociation on the K and Mn promoters.[22,27,34] Another interesting result shown in Table 1 is the enhanced selectivity for long-chain hydrocarbons (C_8+) by the K-promoted Fe catalysts supported on graphene. For example, this selectivity increases from 66.5% to 86.7% in the Fe_{15}-G and $Fe_{15}K_5$-G catalysts, respectively, while maintaining the CH_4 production low (1.5% and 2.6% for the Fe_{15}-G and $Fe_{15}K_5$-G catalysts, respectively). This is consistent with the effect observed in the FTS by iron catalysts supported on activated carbon where the potassium promoter significantly suppresses formation of methane and shifts selectivity to higher-molecular-weight hydrocarbons (C_5+) and alcohols.[58] However, the effect of methane suppression is not observed by adding the Mn promoter to the iron-graphene catalyst, which results in increasing the CH_4 production to 13.5% by the $Fe_{15}Mn_5$-G catalyst as compared with 1.5% and 2.6% for the Fe_{15}-G and $Fe_{15}K_5$-G catalysts, respectively, as shown in Table 1.

dx.doi.org/10.1021/cs4010198 | ACS Catal. 2014, 4, 535−545

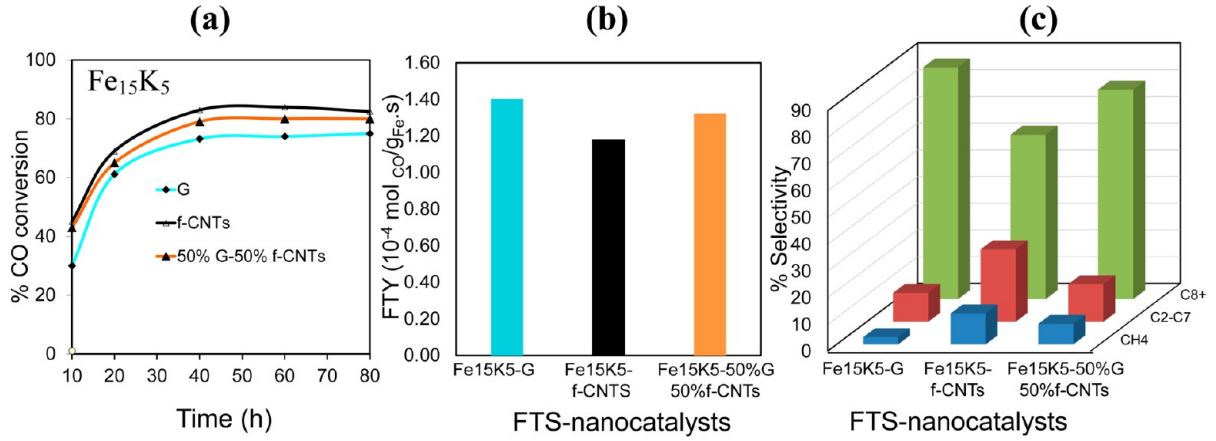

Figure 5. (a) Percent CO conversion vs time on-stream in hours (h) for the $Fe_{15}K_5$ nanocatalyst supported on graphene (G), functionalized carbon nanotubes (f-CNTs), and 50% G−50% f-CNTS at 2500 cm^3 (STP)/(h g) space velocity at 325 °C and 1.5 MPa (220 psi) FT-reactor pressure. (b) Fe time yield, FTY (10^{-4} mol_{CO}/g_{Fe} s) for the $Fe_{15}K_5$ catalyst supported on G, f-CNTs, and G-f-CNTs. (c) Percent selectivity of hydrocarbons produced by the $Fe_{15}K_5$ catalyst supported on G, f-CNTs, and G-f-CNTs.

The relatively high methane production has been reported for other Fe/Mn catalysts supported on carbon materials.[34] For example, an Fe/Mn catalyst prepared using mixed metal carbonyl clusters supported on amorphous carbon black displayed selectivities for CH_4 and C_2−C_4 olefins of 25 and 75 mol %, respectively.[59] Similarly, an FeN/Mn catalyst supported on CNTs showed selectivities for CH_4 and C_2−C_4 olefins of 24 and 44 wt %, respectively, at a temperature of 300 °C and a pressure of 5 bar.[60] High methane production (30%) has also been reported for unsupported Fe−Mn catalysts in which a high C_2−C_4 olefins selectivity (∼50%) was achieved with a 15% Mn in an Fe−Mn catalyst prepared by a coprecipitation method.[61] This catalyst was tested at 350 °C, 15 bar, and a H_2/CO ratio of 2, which are nearly similar to the current experimental conditions used for the graphene-supported catalysts (325 °C, 1.5 MPa, H_2/CO = 2). Therefore, the relatively high methane production observed for the $Fe_{15}Mn_5$-G catalyst (13.5%), as compared with the Fe_{15}-G catalyst (1.5%), is consistent with the performance of other unsupported and supported Mn-containing Fe catalysts.[34,59−61] As pointed out by de Jong, the Anderson−Schulz−Flory (ASF) model predicts a methane selectivity of ∼30% when a high C_2−C_4 olefins selectivity (∼50%) is achieved.[34] The current graphene-supported catalysts show methane selectivity below 15%, which is consistent with their low C_2−C_4 and high C_8+ selectivities, in qualitative agreement with the ASF distribution.[34]

Figure 5 compares the percent CO conversion (Figure 5a), the iron time yield, FTY (Figure 5b), and product selectivity (Figure 5c) for the $Fe_{15}K_5$ catalyst supported on graphene (G), f-CNTs, and a 50% CNTs-G mixed support. Although the $Fe_{15}K_5$ catalyst supported on f-CNTs exhibits the highest percent CO conversion (84%), it shows moderate selectivities (CO_2-free) toward C_2−C_7 (27%) and C_8+ (61.5%) and high selectivities toward CH_4 (11.5%) and CO_2 (CO to CO_2 conversion = 14%), as shown in Table 1. These results are consistent with other Fe catalysts supported on CNTs in which the selectivities for C_2−C_4, C_5+, CH_4, and CO_2 were found to be 41%/54%, 29%/19%, 12%/15%, and 18%/12%, respectively, for the catalysts deposited inside/outside the channels of the CNTs (inner diameters 4−8 nm).[39] This trend is also in general agreement with the results obtained for the Fe nanoparticles supported inside narrow (12 nm) and wide (63 nm) CNTs for which the selectivities for C_2−C_4, C_5+, CH_4, and CO_2 were found to be 37%/47%, 48%/12%, 14.5%/41%, and 18%/12%, respectively, for the catalysts deposited inside the narrow (12 nm)/wide (63 nm) tubes, respectively.[41] From these results, the general pattern of product distribution for the Fe catalysts supported on CNTs for the FTS under the most preferred conditions appears to be the production of (C_2−C_5), (C_5+), CH_4, and CO_2 in the ranges of 27−50%, 29−60%, 12−40%, and 12−18%, respectively, depending on the Fe particle size, CNTs diameters, location of the particles inside or outside the CNTs, the presence of promoters, and the experimental conditions.[35−39,41,42,60]

On the basis of the results shown in Table 1 and Figure 5, it is clear that the performances of the Fe catalysts supported on graphene are quite different from the general pattern of performance of the Fe catalysts supported on CNTs. Taking the $Fe_{15}K_5$-G catalyst as an example, the selectivity toward long-chain hydrocarbons (C_8+) is more than 86% of the CO_2-free products (in comparison with 29−60% for the CNTs-supported catalyst), and the selectivity for the undesired CH_4 and CO_2 products is only 2.6% (in comparison with 12−40% and 12−18% for the Fe catalysts supported on CNTs). Interestingly, by supporting the $Fe_{15}K_5$ catalyst on the f-CNTs-G mixed support, a significant improvement over the f-CNTs support is observed, especially in the product selectivity, as shown in Figure 5c. This indicates that the graphene support plays a critical role in enhancing the C_8+ products and lowering the production of CH_4 and the formation of CO_2.

The significant suppression of CO_2 displayed by the graphene-supported Fe-based catalysts (Table 1) suggests that the WGS is less favorable on graphene than on CNTs. The CO_2 selectivity of the $Fe_{15}K_5$-f-CNTs catalyst was found to be 14% in agreement with the range of 10−20% reported for Fe catalysts supported outside and inside CNTs.[39] However, the CO_2 selectivity of only 2.6% found for the $Fe_{15}K_5$-G catalyst clearly indicates low WGS activity which could be explained by the highly hydrophobic nature of graphene which could retard the approach of water molecules to the graphene surface. In fact recent experimental literature indicates that the contact angle of water on graphene is significantly higher than that on graphite which suggests that graphene could be one of the most hydrophobic surfaces with very weak interaction with the water molecules.[62]

dx.doi.org/10.1021/cs4010198 | ACS Catal. 2014, 4, 535−545

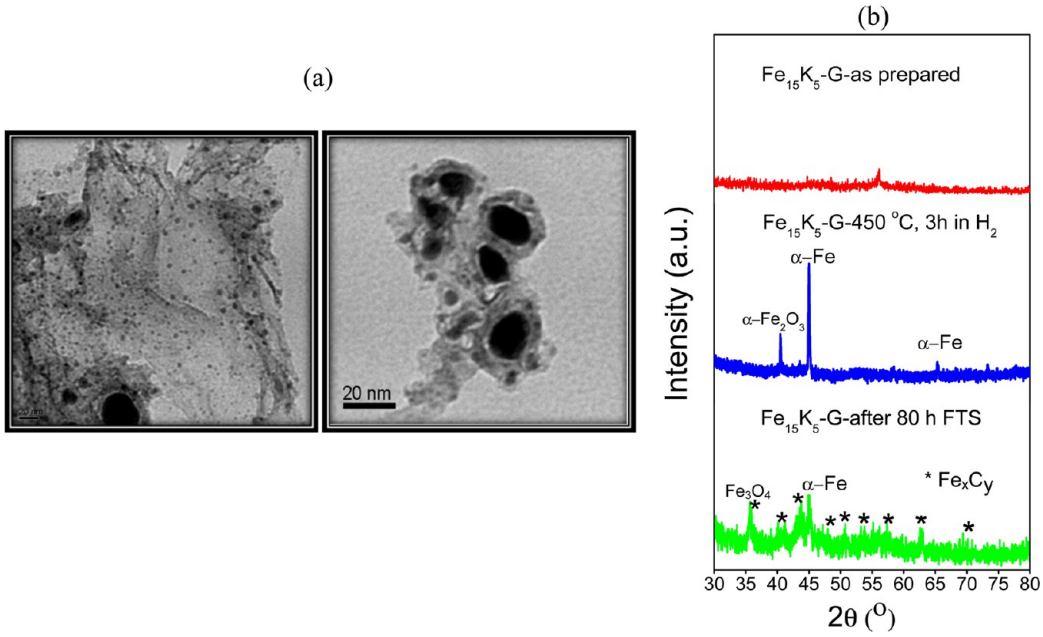

Figure 6. (a) TEM-images of $Fe_{15}K_5$-G after 80 h of FTS. (b) XRD-patterns of the $Fe_{15}K_5$-G catalyst: as-prepared (red), after reduction in H_2 at 450 °C for 3 h (blue), and after 80 h of FTS on stream (green).

The significant suppression of methane and CO_2 and the excellent selectivity toward C_8+ products displayed by the Fe–K/G catalyst confirm the unique role played by graphene in imparting higher catalytic activity and tunable selectivity to the Fe-based FTS catalysts. The high selectivity toward long-chain hydrocarbons is usually related to the rapid formation of an iron carbide active phase.[27,63,64] We postulate that graphene provides favorable kinetics and lower barriers to the formation of the active carbide phase, and therefore, it can result in increasing the rate of chain growth and consequently the production of long-chain hydrocarbons. The interaction of the Fe nanoparticles with the graphene nanosheets similar to CNTs and the wrapping of the edges of the sheets around the Fe nanoparticles could enhance the formation of the active carbide phase, which is critical for the production of long-chain hydrocarbons.[57,63,64]

It is important to discuss the role of mass transfer issues within these different supports. CNTs offer an open structure with abundant access for reactants to diffuse if the iron nanoparticles are deposited on the outer surface of the CNTs; however, it has been established that the catalyst activity is higher if the particles are deposited inside the tubes despite the limited access and the slow diffusion.[38−42] This has been explained by modified electronic interactions between the confined metal nanoparticles and the interior surface of the CNTs.[42] In the case of graphene, the very high surface area nanosheets can crumble, leading to large volumes of limited accessibility. However, since only a few layers of graphene (3–5) are involved, it is likely that nanoparticles anchored to graphene will be covered by one or two layers, where they may experience an environment similar to the particles inside the CNTs but without the narrow tubular effect that could restrict the diffusion of the reactants. This point can be adequately addressed by microporosity measurements of the Fe-based nanoparticle catalysts supported on CNTs and on graphene. Future studies will focus on comparing the transport issues of the catalysts supported on CNTs and on graphene.

Catalyst Activation and Stability. The FT catalyst deactivation is a serious industrial problem that results in loss of catalytic activity or selectivity over time and, thus, can decrease the economic viability of the FTS.[9,11,27] FT-catalyst deactivation is generally due to coke/carbon formation, which is typically enhanced on acidic metal oxide supports, such as Al_2O_3, SiO_2, and ZrO_2, because of their surface acidity.[9,16,17,27−30] To investigate the stability and recyclability of the $Fe_{15}K_5$ graphene-supported catalyst, a sequence of on (325 °C)/off (25 °C) experiments were carried out on the catalyst, and the products were collected and analyzed every 24 h. The CO conversion was found to be nearly constant over the repeated cycles over a total of 96 h, as shown in the SI (Figure S14). The same behavior was observed by increasing the amount of the catalyst used, thus suggesting high stability and excellent recyclability even at higher catalyst concentrations.

The catalyst stability maintained during 80 h of reactor operation at 325 °C and 1.5 MPa pressure provides strong evidence for the potential applications of these catalysts in industrial fluidized-bed reactors. TEM performed on spent $Fe_{15}K_5$-G catalyst following 80 h of operation in the reactor reveals small increases in the particle's size and the degree of agglomeration, as shown in Figure 6a. The TEM images also suggest the formation of a carbide shell surrounding the Fe core of the catalyst. The formation of Fe_xC_y iron carbide was confirmed by the XRD data of the catalyst obtained after 80 h of reaction time, as shown in Figure 6b. Similar XRD data showing the formation of Fe_xC_y iron carbide were obtained for the $Fe_{20}K_{10}$-G catalyst after 80 h of reaction time, as shown in Figure S8 (SI). This suggests that the graphene support could facilitate the formation of the carbide active phase that enhances the stability and recyclability of the catalyst.

It is well-established that several iron carbide phases, such as Fe_3C, Fe_5C_2, Fe_2C, and Fe_4C, are usually present during FTS involving iron-based catalysts.[27] Several studies suggest that Fe_5C_2 (Hägg iron carbide) is the real active phase, not metallic iron,[27,63,64] and deactivation of the catalyst occurs when the Fe_5C_2 phase is gradually converted into inactive carbon

dx.doi.org/10.1021/cs4010198 | ACS Catal. 2014, 4, 535−545

deposits.[27] Most of the observed XRD peaks shown in Figures 6b and S8 (SI) could be assigned to the Fe_5C_2 active phase, which is known to have high activity and selectivity toward the formation of long-chain hydrocarbons (C_8+).[27,64] Recently, Fe_5C_2 nanoparticles were synthesized and shown to exhibit intrinsic catalytic activity in FTS, thus demonstrating that Fe_5C_2 is an active phase for FTS.[64] Interestingly, the synthesized Fe_5C_2 nanoparticles have a core−shell morphology similar to the particles observed after 80 h of reaction time on the $Fe_{15}K_5$-G catalyst, as shown by the TEM images in Figure 6a. This and the XRD pattern of the spent $Fe_{15}K_5$-G catalyst after 80 h of FTS reaction (Figure 6b) provide strong evidence for the formation of the Fe_5C_2 active phase during the FTS on the graphene-supported Fe catalysts.

Correlation with Surface Defects in the Graphene Support. Our results indicate that the graphene-supported FT catalysts have higher activity and significant selectivity toward the production of long-chain hydrocarbons in addition to excellent stability and recyclability. The origin of the enhancement in activity and selectivity of the graphene-supported FT catalysts is not fully understood. Traditional surface area and dispersion factors may not account for this activity, and the emergence of electronic factors that fundamentally alter interactions with the support need to be investigated. We postulate that the defect sites on the surface of graphene provide an excellent environment for the nucleation of surface-active metal nanoparticles and, as a result, play a major role in imparting exceptional catalytic properties and stability to the metal-graphene catalysts. It is now well established that the chemical reduction of GO results in the formation of graphene nanosheets with a significant number of defect sites, including vacancies, disorder, defective edges, and others.[65−67] The use of MWI in our synthesis of the graphene-supported catalysts is expected to enhance the formation of graphene defects, especially in the presence of metal nanoparticles due to the nonequilibrium heating and the formation of energetic hot spots.[48,51]

Raman spectroscopy is one of the most useful techniques that can identify the nature of defects and disorder in the graphene and metal−graphene nanosheets.[68−70] To gain information on the extent of defects in the Fe-based catalysts supported on graphene, we have measured the Raman spectra of GO and graphene formed after the hydrazine hydrate−MWI-assisted chemical reduction of GO in the absence and presence of the metal ion precursors (Fe, K, and Mn nitrates), as shown in Figure 7.

The Raman spectrum of GO exhibits the characteristic G band (1594 cm^{-1}) and the D band (1354 cm^{-1}) with a D-to-G intensity ratio of about 0.70. The G band arises from the vibration of the sp^2 bonded carbon atoms, and the D band is attributed to structural disorder at defect sites, with the D/G ratio usually taken as a measure of the quality of the graphitic structures, because for highly ordered pyrolitic graphite, this ratio approaches zero.[68−70] Following the MWI of GO in the presence of HH, the D/G ratio decreases to 0.27, indicating a significant decrease in the degree of disorder and defect sites in the RGO. In addition, a small shoulder, identified as the D′ band, appears around 1612 cm^{-1} and is attributed to finite size effects.[68−70] It is clear that no decrease in the intensity of the D band relative to the G band is observed following the MWI of the GO−Fe nitrate−K nitrate or the GO−Fe nitrate−Mn nitrate solutions, as shown in Figure 7. In fact, the D/G ratio increases from 0.27 in RGO to 0.46 or to 0.51 after the MWI of

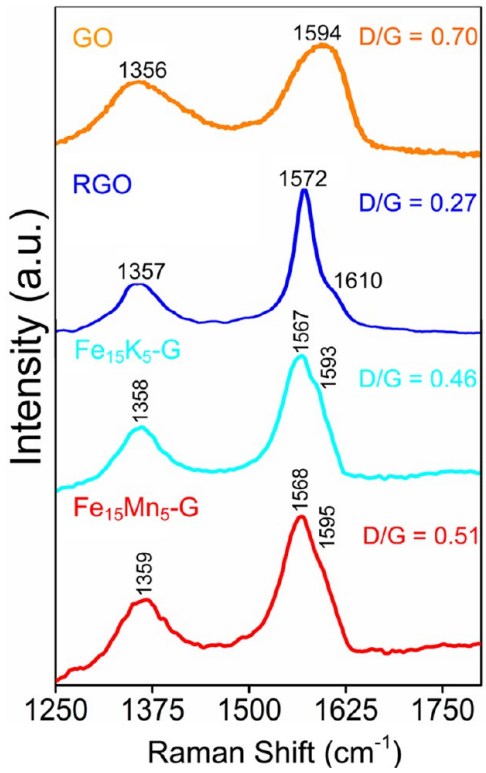

Figure 7. Raman spectra of GO, graphene prepared by the hydrazine hydrate reduction of GO under microwave irradiation (GO−HH−MWI) and the $Fe_{15}K_5$-G and $Fe_{15}Mn_5$-G catalysts.

the GO solutions containing iron nitrate + potassium nitrate or iron nitrate + manganese nitrate, respectively. The increase in the D/G intensity ratio in the $Fe_{15}K_5$-G and $Fe_{15}Mn_5$-G catalysts is taken as evidence for the presence of more structural defects in the graphene lattice induced by MWI of GO in the presence of Fe−K or Fe−Mn nanoparticles. It is also clear that the intensity of the D′ shoulder is enhanced significantly and shifts to lower frequency in the spectra of the $Fe_{15}K_5$-G and $Fe_{15}Mn_5$-G catalysts, indicating the increase in the defect density in the graphene lattice. These defect sites act as favorable nucleation sites for the formation of the Fe-based nanoparticle catalysts that can be anchored to the graphene surface, thus reducing the mobility of these catalysts and decreasing their tendency to agglomerate.

Metal−support interactions involve both electronic and geometric factors, but the electronic interactions could be more significant in the case of graphene support because of the possibility of charge transfer between the graphene support and the iron nanoparticles. The resulting metal−support interactions can induce significant changes in adsorbate binding energies and, thus, significantly influence reaction thermodynamics and kinetics.

CONCLUSIONS

In summary, the Fe−K and Fe−Mn catalysts supported on graphene exhibit high FTS activity and selectivity toward higher hydrocarbons. The graphene-supported $Fe_{15}K_5$ catalyst exhibits a unique tendency toward minor formation of CH_4 and CO_2 as compared with CNTs-supported catalysts. The water-gas shift activity is significantly reduced on the graphene support as compared with CNTs, and as a result, the formation of CO_2 is significantly reduced. The remarkable differences in activity and

dx.doi.org/10.1021/cs4010198 | ACS Catal. 2014, 4, 535−545

product selectivity of the $Fe_{15}K_5$ catalyst supported on graphene and CNTs provide strong evidence for the accessibility of the active phase of the Fe catalyst supported on graphene to the reactants and to the unique properties of the graphene support in imparting such high activity and selectivity to the Fe-based catalysts. The high activity of the graphene-supported, Fe-based catalysts may have been associated with well-dispersed nanoparticles on the large surface area of graphene and with enhanced catalyst-graphene interactions attributed to the presence of defect sites that anchor the nanoparticles to the graphene surface. Evidence is presented for the formation of the active Fe_5C_2 iron carbide phase during the FTS on the graphene-supported Fe catalysts. Given the activity, selectivity, and stability of the new graphene-supported Fe-based nanoparticle catalysts, their industrial application appears to be promising. Further maximization of the C_8+ hydrocarbons and reduction of the CH_4 and CO_2 products by tuning catalyst−graphene interactions through careful engineering of the defect sites on graphene will allow us to understand the nature of these interactions and to further enhance the performance of these catalysts for the production of liquid fuels.

■ ASSOCIATED CONTENT

Supporting Information

Details of the catalyst preparation methods and the synthesis of f-CNTs; TEM images and particle size distributions of Fe-based nanoparticle catalysts supported on graphene; XRD and XPS data of the as-prepared, activated, and spent $Fe_{20}K_{10}$-G, $Fe_{15}Mn_5$-G, and $Fe_{15}Mn_5K_5$-G catalysts; XRD and Raman spectra of FeK-CNTs catalysts; FTS-recycling duration of the $Fe_{15}K_5$-G catalyst at 325 °C; photograph of the fixed-bed microreactor; and details of the product analysis (Figures S1−S14). This material is available free of charge via the Internet at http://pubs.acs.org.

■ AUTHOR INFORMATION

Corresponding Author

*E-mail: mselshal@vcu.edu.

Notes

The authors declare no competing financial interest.

†(M.S.E.-S.) Also affiliated with the Department of Chemistry, King Abdulaziz University, Jeddah 21589, Saudi Arabia.

■ ACKNOWLEDGMENTS

The authors acknowledge financial support from the National Science Foundation (CHE-0911146) and Afton Chemical Corporation. We thank Drs. Tze-Chi Jao, Allen Aradi, Huifang Shao, and Zack MacAfee (Afton Chemical) for their help with FTS reactor and facilities. We thank Prof. James Terner (VCU) for the help with the Raman measurements.

■ REFERENCES

(1) NAS-NAE-NRC (National Academy of Sciences-National Academy of Engineering-National Research Council). *America's Energy Future: Technology and Transformation*; The National Academies Press: Washington, D.C., 2009.

(2) Cahen, D.; Lubomirsky, I. *Mater. Today* **2008**, *11*, 16−20.

(3) *Liquid Transportation Fuels from Coal and Biomass: Technological Status, Costs, and Environmental Impacts, America's Energy Future Panel on Alternative Liquid Transportation Fuels*; The National Academies Press: Washington, D.C., 2010.

(4) Bull, T. E. *Science* **1999**, *285*, 1209.

(5) Metzger, J. O. *Angew. Chem., Int. Ed.* **2006**, *45*, 696−698.

(6) Kunkes, E. L.; Simonetti, D. A.; West, R. M.; Serrano-Ruiz, J. C.; Gärtner, C. A.; Dumesic, J. A. *Science* **2008**, *322*, 417−421.

(7) Vispute, T. P.; Zhang, H.; Sanna, A.; Xiao, R.; Huber, G. W. *Science* **2010**, *330*, 1222−1227.

(8) Ngo, H. L.; Zafiropoulos, N. A.; Foglia, T. A.; Samulski, E. T.; Lin, W. *Energy Fuels* **2008**, *22*, 626−634.

(9) Steynberg, A. P., Dry, M. E., Eds.; *Fischer−Tropsch Technology*; Elsevier: Amsterdam, 2004.

(10) Anderson, R. B. *The Fischer−Tropsch Synthesis*; Academic Press: Orlando, FL, 1984.

(11) De Klerk, A. *Green Chem.* **2007**, *9*, 560−565.

(12) Khodakov, A. Y.; Chu, W.; Fongarland, P. *Chem. Rev.* **2007**, *107*, 1692−1744.

(13) De Klerk, A. *Energy Fuels* **2009**, *23*, 4593−4604.

(14) Dupain, X.; Krul, R. A.; Schaverien, C. J.; Makkee, M.; Moulijn, J. A. *Appl. Catal., B* **2006**, *63*, 277−295.

(15) Davis, B. H. *Catal. Today* **2008**, *141*, 25−33.

(16) Eggenhuisen, T. M.; den Breejen, J. P.; Verdoes, D.; de Jongh, P. E.; de Jong, K. P. *J. Am. Chem. Soc.* **2010**, *132*, 18318−18325.

(17) Borg, O.; Hammer, N.; Eri, S.; Lindvag, O. A.; Myrstad, R.; Blekkan, E. A.; Ronning, M.; Rytter, E.; Holmen, A. *Catal. Today* **2009**, *142*, 70−77.

(18) Barrault, J.; Forguy, C.; Menezo, J. C.; Maurel, R. *React. Kinet. Catal. Lett.* **1980**, *15*, 153.

(19) Sommen, A. P. B.; Stoop, F.; van der Wiele, K. *Appl. Catal.* **1985**, *14*, 277−288.

(20) Jones, V. K.; Neubauer, L. R.; Bartholomew, C. H. *J. Phys. Chem.* **1986**, *90*, 4832−4839.

(21) Bukur, D. B.; Lang, X.; Mukesh, D.; Zimmerman, W. H.; Rosynek, M. P.; Li, C. *Ind. Eng. Chem. Res.* **1990**, *29*, 1588−1599.

(22) Xu, L.; Wang, Q.; Xu, Y.; Huang, J. *Catal. Lett.* **1995**, *31*, 253−266.

(23) Shroff, M. D.; Kalakkad, D. S.; Coulter, K. E.; Kohler, S. D.; Harrington, M. S.; Jackson, N. B.; Sault, A. G.; Datye, A. K. *J. Catal.* **1995**, *156*, 185−207.

(24) Cubeiroa, M. L.; Lópeza, C. M.; Colmenaresa, A.; Teixeiraa, L.; Goldwassera, M. R.; Pérez-Zuritaa, M. J.; Machadoa, F.; González-Jiménezа, F. *Appl. Catal., A* **1998**, *167*, 183−193.

(25) Li, S.; O'Brien, R. J.; Meitzner, G. D.; Hamdeh, H.; Davis, B. H.; Iglesia, E. *Appl. Catal., A* **2001**, *219*, 215−222.

(26) Herranz, T.; Rojas, S.; Perez-Alonso, F. J.; Ojeda, M.; Terreros, P.; Fierro, J. L. G. *J. Catal.* **2006**, *243*, 199−211.

(27) De Smit, E.; Weckhuysen, B. M. *Chem. Soc. Rev.* **2008**, *37*, 2758−2781.

(28) Kang, S. H.; Bae, J. W.; Prasad, P. S. S.; Park, S. J.; Wu, K. J.; Jun, K. W. *Catal. Lett.* **2009**, *130*, 630−636.

(29) Torres Galvis, H. M.; Bitter, J. H.; Khare, C. B.; Ruitenbeek, M.; Dugulan, A. J.; de Jong, K. P. *Science* **2012**, *335*, 835−838.

(30) Wielers, A. F. H.; Kock, A. J. H. M.; Hop, C. E. C. A.; Geus, J. W.; van der Kraan, A. M. *J. Catal.* **1989**, *117*, 1−18.

(31) Torres Galvis, H. M.; Bitter, J. H.; Davidian, T.; Ruitenbeek, M.; Dugulan, A. I.; Krijn, P.; de Jong, K. P. *J. Am. Chem. Soc.* **2012**, *134*, 16207−16215.

(32) Bezemer, G. L.; Bitter, J. H.; Kuipers, H. P. C. E.; Oosterbeek, H.; Holewijin, J. E.; Xu, X.; Kapteijin, F.; Jos van Dillen, A.; de Jong, K. P. *J. Am. Chem. Soc.* **2006**, *128*, 3956−3964.

(33) Breejen, J. P.; Radstake, P. B.; Bezemer, G. L.; Bitter, J. H.; Froseth, V.; Holmen, A.; de Jong, K. P. *J. Am. Chem. Soc.* **2009**, *131*, 7197−7203.

(34) Torres, H. M.; de Jong, K. P. *ACS Catal.* **2013**, *3*, 2130−2149.

(35) Schutle, H. J.; Graf, B.; Xia, W.; Muhler, M. *ChemCatChem* **2012**, *4*, 350−355.

(36) Van Steen, E.; Prinsloo, F. F. *Catal. Today* **2002**, *71*, 327−334.

(37) Guczi, L.; Stefler, G.; Geszti, O.; Koppany, Zs.; Konya, Z.; Molnar, E.; Urban, M.; Kiricsi, I. *J. Catal.* **2006**, *244*, 24.

(38) Chen, W.; Pan, X.; Bao, X. *J. Am. Chem. Soc.* **2007**, *129*, 7421−7426.

(39) Chen, W.; Fan, Z.; Pan, X.; Bao, X. *J. Am. Chem. Soc.* **2008**, *130*, 9414−9419.
(40) Abbaslou, R. M. M.; Tavassoli, A.; Soltan, J.; Dalai, A. K. *Appl. Catal., A* **2009**, *367*, 47−52.
(41) Abbaslou, R. M. M.; Soltan, J.; Dalai, A. K. *Appl. Catal., A* **2010**, *379*, 129−134.
(42) Pan, X.; Bao, X. *Acc. Chem. Res.* **2011**, *44*, 553−562.
(43) Schaetz, A.; Zeltner, M.; Stark, W. J. *ACS Catal.* **2012**, *2*, 1267−1284.
(44) Su, D. S.; Perathoner, S.; Centi, G. *Chem. Rev.* **2013**, *113*, 5782−5816.
(45) Zhao, H.; Zhu, Q.; Gao, Y.; Zhai, P.; Ma, D. *Appl. Catal., A* **2013**, *456*, 223−239.
(46) Kamat, P. V. *J. Phys. Chem. Lett.* **2010**, *1*, 520−527.
(47) Jasuja, K.; Linn, J.; Melton, S.; Berry, V. *J. Phys. Chem. Lett.* **2010**, *1*, 1853−1860.
(48) Siamaki, A. R.; Khder, A. E. R. S.; Abdelsayed, V.; El-Shall, M. S.; Gupton, B. F. *J. Catal.* **2011**, *279*, 1−11.
(49) Moussa, S.; Abdelsayed, V.; El-Shall, M. S. *Chem. Phys. Lett.* **2011**, *510*, 179−184.
(50) Moussa, S.; Siamaki, A. R.; Gupton, B. F.; El-Shall, M. S. *ACS Catal.* **2012**, *2*, 145−154.
(51) El-Shall, M. S. Heterogeneous Catalysis by Metal Nanoparticles Supported On Graphene. In *Graphene: Synthesis, Properties and Phenomena*; Rao, C. N. R., Sood, A. K., Eds.; Wiley-VCH: Weinheim, 2013; Chapter 10; pp 303−338.
(52) Hassan, H. M. A.; Abdelsayed, V.; Khder, A. E. R.; AbouZeid, K. M.; Terner, J.; El-Shall, M. S.; Al-Resayes, S. I.; El-Azhary, A. A. *J. Mater. Chem.* **2009**, *19*, 3832−3837.
(53) Abdelsayed, V.; Aljarash, A.; El-Shall, M. S. *Chem. Mater.* **2009**, *21*, 2825−2834.
(54) Herring, N. P.; AbouZeid, K.; Mohamed, M. B.; Pinsk, J.; El-Shall, M. S. *Lagmuir* **2011**, *27*, 15146−15154.
(55) Hummers, W. S., Jr.; Offerman, R. E. *J. Am. Chem. Soc.* **1958**, *80*, 1339−1340.
(56) Panchakarla, L. S.; Govindaraj, A. *Bull. Mater. Sci.* **2007**, *30*, 23−29.
(57) Yu, G.; Sun, B.; Pei, Y.; Xie, S.; Yan, S.; Qiao, M.; Fan, K.; Zhang, X.; Zong, B. *J. Am. Chem. Soc.* **2010**, *132*, 935−937.
(58) Ma, W.; Kugler, E. L.; Dadyburjor, D. B. *Energy Fuels* **2007**, *21*, 1832−1842.
(59) Venter, J.; Kaminsky, M.; Geoffroy, G. L.; Vannice, M. A. *J. Catal.* **1987**, *103*, 450−465.
(60) Yang, Z.; Pan, X.; Wang, J.; Bao, X. *Catal. Today* **2012**, *186*, 121−127.
(61) Wang, C.; Wang, Q.; Sun, X.; Xu, L. *Catal. Lett.* **2006**, *105*, 93−101.
(62) Wang, S. R.; Zhang, Y.; Abidi, N.; Cabrales, L. *Langmuir* **2009**, *25*, 11078−11081.
(63) De Smit, E.; Cinquni, F.; Beale, A. M.; Safonova, O. V.; Van Beek, W.; Sautet, P.; Weckhuysen, B. M. *J. Am. Chem. Soc.* **2010**, *132*, 14928−14941.
(64) Yang, C.; Zhao, H.; Hou, Y.; Ma, D. *J. Am. Chem. Soc.* **2012**, *134*, 15814−15821.
(65) Bagri, A.; Mattevi, C.; Acik, M.; Chabal, Y. J.; Chhowalla, M.; Shenoy, V. B. *Nat. Chem.* **2010**, *2*, 581−587.
(66) Banhart, F.; Kotakoski, J.; Krashennnikov, A. V. *ACS Nano* **2011**, *5*, 26−41.
(67) Kim, G.; Jhi, S.-H. *ACS Nano* **2011**, *5*, 805−810.
(68) Ferrari, A. C. *Solid State Commun.* **2007**, *446*, 60−63.
(69) Dresselhaus, M. S.; Jorio, A.; Hofmann, M.; Dresselhaus, G.; Saito, R. *Nano Lett.* **2010**, *10*, 751−758.
(70) Cancado, L. G.; Jorio, A.; Martins Ferreira, E. H.; Stavale, F.; Achete, C. A.; Capaz, R. B.; Moutinho, M. V. O.; Lombardo, A.; Kulmala, T. S.; Ferrari, A. C. *Nano Lett.* **2011**, *11*, 3190−3196.